Polarized states and domain walls in spinor Bose-Einstein condensates

H. E. Nistazakis,[1] D. J. Frantzeskakis,[1] P. G. Kevrekidis,[2] B. A. Malomed,[3] R. Carretero-González,[4] and A. R. Bishop[5]

[1]*Department of Physics, University of Athens, Panepistimiopolis, Zografos, Athens 15784, Greece*
[2]*Department of Mathematics and Statistics, University of Massachusetts, Amherst, Massachusetts 01003-4515, USA*
[3]*Department of Interdisciplinary Studies, Faculty of Engineering, Tel Aviv University, Tel Aviv 69978, Israel*
[4]*Nonlinear Dynamical Systems Group, Department of Mathematics and Statistics and Computational Science Research Center, San Diego State University, San Diego, California 92182-7720, USA*
[5]*Theoretical Division and Center for Nonlinear Studies, Los Alamos National Laboratory, Los Alamos, New Mexico 87545, USA*

We study spin-polarized states and their stability in the antiferromagnetic phase of spinor ($F=1$) quasi-one-dimensional Bose-Einstein condensates. Using analytical approximations and numerical methods, we find various types of polarized states, including patterns of the Thomas-Fermi type, structures featuring a pulse in one component inducing a hole in the other components, states with holes in all three components, and domain walls (DWs). The stability analysis based on the Bogoliubov–de Gennes equations reveals intervals of weak oscillatory instability in families of these states, except for the DWs, which are always stable. The development of the instabilities is examined by means of direct simulations.

I. INTRODUCTION

The development of the far-off-resonant optical techniques for trapping ultracold atomic gases has opened new directions in the studies of Bose-Einstein condensates (BECs). By means of these techniques, atoms can be confined regardless of their hyperfine (spin) state, thus avoiding freezing the atom's spin degree of freedom and paving the way for the study of the collective spin dynamics [1]. One of the major achievements in this direction was the experimental creation of *spinor* BECs [2,3]. The spinor condensate formed by atoms with spin F is described by a $(2F+1)$-component macroscopic (mean-field) wave function, which gives rise to various phenomena that are not present in single-component BECs, including formation of spin domains [4], spin textures [5], and multicomponent (vectorial) solitons of bright [6–8], dark [9], gap [10], and bright-dark [11] types.

Generally, the dynamics of the spinor $F=1$ BEC is spin-mixing [12]. However, there also exist *spin-polarized* states of the system, which are stationary solutions of the corresponding system of Gross-Pitaevskii (GP) equations [13,14]. The stability of such polarized states is different for the two distinct types of the $F=1$ condensates, namely the *ferromagnetic* (FM), such as in [87]Rb, and *polar* [alias *antiferromagnetic* (AFM)], such as [23]Na, ones, where the spin-dependent interactions are, respectively, attractive and repulsive. Accordingly, as demonstrated in Refs. [15] and [7], spin-polarized states are modulationally stable (unstable) in the AFM (FM) condensates.

In this work, we focus on AFM spinor condensates, and study, in particular, spin-polarized states of the spinor BEC of [23]Na atoms. Assuming that this spinor system is confined in a strongly anisotropic trap, we first present the respective system of three coupled quasi-one-dimensional (1D) GP equations. Then, employing the so-called single-mode approximation, which expresses the profiles of all three components of the spinor condensate in terms of a single spatial

mode [12,15], we use analytical and numerical methods to find the spin-polarized states of the system and study their stability via the Bogoliubov–de Gennes (BdG) equations (i.e., the linearization of the GP equations for small perturbations; this approach does not take into regard incoherent perturbations involving "vapor" fluctuations above the condensate, but the addition of the "vapor" perturbations does not usually affect the stability of localized states in BECs [16]). The simplest possible form of these states is based on the Thomas-Fermi (TF) configurations (in each hyperfine component). We also present other spin-polarized states, including those in which one component is pulse-shaped, inducing a hole in the other two components, and structures with holes in all three components. Families of all these states feature regions of weak oscillatory instabilities, with values of the normalized instability growth rate $\lesssim 10^{-3}$. Development of the oscillatory instabilities is examined by means of direct simulations. It is found that the unstable structures with a hole in one component get weakly deformed, while the unstable states with holes in all the three components suffer stronger deformations. If three initially spatially separated components, kept in different harmonic traps, are placed in a single trap, spin domain-wall (DW) patterns are formed. A family of the DW solutions exists and is fully stable if, for a fixed value of the trap's strength, the chemical potential (or the number of atoms) exceeds a certain critical value.

The paper is organized as follows. Section II presents the model. Section III deals with the TF states. In Secs. IV and V we examine three-component structures with one and multiple holes, respectively (including their stability). Finally, conclusions are presented in Sec. VI.

II. MODEL AND SETUP

In the framework of the mean-field approach, a spinor BEC with $F=1$ is described by a vectorial order parameter, $\Psi(\mathbf{r},t)=[\Psi_{-1}(\mathbf{r},t),\Psi_0(\mathbf{r},t),\Psi_{+1}(\mathbf{r},t)]^T$, with the different

fields corresponding to three values of the vertical component of the spin, $m_F = -1, 0, +1$. Assuming that this condensate is loaded into a strongly anisotropic trap, with holding frequencies $\omega_x \ll \omega_\perp$, we assume, as usual, that the wave functions are separable, $\Psi_{0,\pm 1} = \psi_{0,\pm 1}(x)\psi_\perp(y,z)$, where the transverse components $\psi_\perp(y,z)$ represent the ground state of the respective harmonic oscillator. Then, following the standard approach [17] of averaging the coupled 3D GP equations in the transverse plane (y,z), we arrive at the system of coupled 1D equations for the longitudinal components of the wave functions (see Refs. [6,7,9–11]):

$$i\hbar\partial_t\psi_{\pm 1} = \hat{H}_{\text{si}}\psi_{\pm 1} + c_2^{(1D)}(|\psi_{\pm 1}|^2 + |\psi_0|^2 - |\psi_{\mp 1}|^2)\psi_{\pm 1} + c_2^{(1D)}\psi_0^2\psi_{\mp 1}^*, \tag{1}$$

$$i\hbar\partial_t\psi_0 = \hat{H}_{\text{si}}\psi_0 + c_2^{(1D)}(|\psi_{-1}|^2 + |\psi_{+1}|^2)\psi_0 + 2c_2^{(1D)}\psi_{-1}\psi_0^*\psi_{+1}, \tag{2}$$

where the asterisk denotes complex conjugate and $\hat{H}_{\text{si}} \equiv -(\hbar^2/2m)\partial_x^2 + \frac{1}{2}m\omega_x^2 x^2 + c_0^{(1D)}n_{\text{tot}}$ is the spin-independent part of the Hamiltonian, with $n_{\text{tot}} = |\psi_{-1}|^2 + |\psi_0|^2 + |\psi_{+1}|^2$ being the total density (m is the atomic mass). The nonlinearity coefficients have an effectively 1D form, namely $c_0^{(1D)} = c_0/2\pi a_\perp^2$ and $c_2^{(1D)} = c_2/2\pi a_\perp^2$, where $a_\perp = \sqrt{\hbar/m\omega_\perp}$ is the transverse harmonic-oscillator length which determines the size of the transverse ground state. The coupling constants c_0 and c_2 account for, respectively, the mean-field spin-independent and spin-dependent binary interactions between identical spin-1 bosons,

$$\{c_0, c_2\} = (4\pi\hbar^2/3m)\{(a_2 + a_0), (a_2 - a_0)\}, \tag{3}$$

where a_0 and a_2 are the s-wave scattering lengths in combined symmetric collision channels corresponding to values of the total spin $f = 0$ and 2. The spinor condensate with $c_2 < 0$ and $c_2 > 0$ is of the FM and AFM types, such as, respectively, ^{87}Rb and ^{23}Na [13,18].

Measuring time, length, and density in units of $\hbar/c_0^{(1D)}n_0$, $\hbar/\sqrt{mc_0^{(1D)}n_0}$, and peak density n_0, we cast Eqs. (1) and (2) in the dimensionless form

$$i\partial_t\psi_{\pm 1} = H_{\text{si}}\psi_{\pm 1} + \delta(|\psi_{\pm 1}|^2 + |\psi_0|^2 - |\psi_{\mp 1}|^2)\psi_{\pm 1} + \delta\psi_0^2\psi_{\mp 1}^*, \tag{4}$$

$$i\partial_t\psi_0 = H_{\text{si}}\psi_0 + \delta(|\psi_{-1}|^2 + |\psi_{+1}|^2)\psi_0 + 2\delta\psi_{-1}\psi_0^*\psi_{+1}, \tag{5}$$

where $H_{\text{si}} \equiv -\frac{1}{2}\partial_x^2 + \frac{1}{2}\Omega^2 x^2 + n_{\text{tot}}$, the normalized trap's strength is

$$\Omega = \frac{3}{2(a_0 + 2a_2)n_0}\left(\frac{\omega_x}{\omega_\perp}\right), \tag{6}$$

and the FM or AFM character of the spinor condensate corresponds, respectively, to $\delta < 0$ and $\delta > 0$, with

$$\delta \equiv \frac{c_2^{(1D)}}{c_0^{(1D)}} = \frac{a_2 - a_0}{a_0 + 2a_2}. \tag{7}$$

For spin-1 ^{87}Rb and ^{23}Na atoms, this parameter is $\delta = -4.66 \times 10^{-3}$ [19] and $\delta = 3.14 \times 10^{-2}$ [20], respectively.

We note that the above mean-field description of the system, based on the three coupled GP Eqs. (4) and (5), is accurate only for temperatures well below the critical transition temperature T_c. In such a case, the effects of quantum or thermal fluctuations on the spinor BEC may be ignored. However, it is possible to study the dynamics of spin-1 atoms in finite temperatures adopting, e.g., a Hartree-Fock-Popov type of approximation [21], or a BdG description of the thermal cloud [22,23]. In the present case, however, such a detailed study of the effect of the temperature is beyond our present scope.

Spin-polarized states of the system, characterized by a constant population of each spin component, can be constructed in the form of

$$\psi_j = \sqrt{n_j(x)}\exp(i\theta_j - i\mu_j t), \quad j = -1, 0, +1, \tag{8}$$

where n_j and θ_j are densities and phases of the components and μ_j are their chemical potentials. Substituting this in Eqs. (4) and (5), it is readily found that conditions for the existence of the spin-polarized states are

$$2\mu_0 = \mu_{-1} + \mu_{+1},$$

$$\Delta\theta \equiv 2\theta_0 - \theta_{+1} - \theta_{-1} = 0 \quad \text{or} \quad \pi. \tag{9}$$

Below, we assume that the chemical potentials for all components are equal: $\mu \equiv \mu_{-1} = \mu_0 = \mu_{+1}$.

To analyze the stability of a stationary spin-polarized state, $\Psi_s(x) = [\tilde{\psi}_{-1}(x), \tilde{\psi}_0(x), \tilde{\psi}_{+1}(x)]^T$, we perform linearization around the unperturbed state, assuming a perturbed solution,

$$\psi_j(x,t) = \{\tilde{\psi}_j(x) + \epsilon[u_j(x)e^{-\lambda t} + v_j^*(x)e^{\lambda^* t}]\}e^{-i\mu t}, \tag{10}$$

where u_j and v_j represent infinitesimal perturbations with eigenvalues $\lambda \equiv \lambda_r + i\lambda_i$. Then, the solution of the ensuing BdG equations for λ and associated eigenfunctions u_j, v_j^* provides complete information about the stability of the underlying stationary state, Ψ_s. Whenever it is unstable, we will also examine its evolution through direct simulations of the GP Eqs. (4) and (5), using a finite-difference scheme in space and the fourth-order Runge-Kutta integrator in time. Typically, in the simulations the unstable state is initially perturbed by a uniformly distributed random perturbation of relative amplitude 5×10^{-4}.

At this point, and in this dimensionless 1D setting under consideration, it is also useful to introduce the distributions of the local spin average defined as (see, e.g., Refs. [24] and [8] for the 1D case)

$$f_x(x;t) = \sqrt{2}\,\text{Re}[\psi_0(\psi_{+1}^* + \psi_{-1}^*)]/n_{\text{tot}}, \tag{11}$$

$$f_y(x;t) = -\sqrt{2}\,\text{Im}[\psi_0^*(\psi_{+1} - \psi_{-1})]/n_{\text{tot}}, \tag{12}$$

$$f_z(x;t) = (|\psi_{+1}|^2 - |\psi_{-1}|^2)/n_{\text{tot}}, \tag{13}$$

with the total normalized mean-field spin given by $f(x;t) = \sqrt{f_x^2 + f_y^2 + f_z^2}$. For the spin-polarized states that we will present below, the y component of the mean-field spin will always be $f_y = 0$; additionally, in most cases (apart from one

pertaining to a certain domain-wall type—see Sec. V) the z component will also be $f_z=0$. Thus, in most cases, the total mean-field spin will be $f=|f_x|$.

Finally, to estimate relevant physical parameters, we assume a spinor condensate of ^{23}Na atoms with 1D peak density $n_0=10^8$ m^{-1}, confined in the harmonic trap with transverse and longitudinal frequencies $\omega_\perp=2\pi\times230$ Hz and $\omega_x=2\pi\times13$ Hz. In this case, the normalized trap strength is $\Omega=0.1$ (this value is kept fixed throughout this work), while the number of atoms, N, depends on chemical potential μ and the particular form of spin-polarized states. Typically, we take μ in interval $1\leq\mu\leq5$, which corresponds to values of N in the range of $3.5\times10^3\leq N\leq3.5\times10^4$ atoms. For instance, at $\mu=2$ the number of atoms is $N\sim10^4$; in this case, the normalized time and space units correspond, respectively, to 1.2 ms and 1.83 μm.

III. THOMAS-FERMI SPIN-POLARIZED STATES

The simplest spin-polarized states can be found in the framework of the *single-mode approximation* [12,15]. In anticipation of the fact that the three components $\sqrt{n_j(x)}$ may be close to eigenmodes of a single effective potential, induced by a combination of the trap and nonlinearity, we introduce the ansatz $n_j(x)=q_j n(x)$. Here, the coefficients q_j are the populations of each spin component in the steady state, subject to the normalization condition $q_{-1}+q_0+q_{+1}=1$. Then, Eqs. (4) and (5) lead to the following system:

$$\left[\hat{L}+\delta\left(1+\sqrt{\frac{q_{\mp1}}{q_{\pm1}}}(sq_0-2\sqrt{q_{-1}q_{+1}})\right)n\right]\sqrt{n}=0, \quad (14)$$

$$[\hat{L}+\delta(1-q_0+2s\sqrt{q_{-1}q_{+1}})n]\sqrt{n}=0, \quad (15)$$

where $\hat{L}\equiv-\mu-\frac{1}{2}\partial_x^2+\frac{1}{2}\Omega^2x^2+n$ and $s=\pm1$ for $\Delta\theta=0$ or $\Delta\theta=\pi$, respectively. In fact, Eqs. (14) and (15) are two equations for a single function, and it can be readily checked that they are tantamount to a single equation, viz.

$$\left(-\mu-\frac{1}{2}\partial_x^2+\frac{1}{2}\Omega^2x^2+pn\right)\sqrt{n}=0, \quad (16)$$

if the following relations are imposed upon populations q_0 and $q_{\pm1}$, and the constant p in Eq. (16) is defined as follows:

$$p\equiv1+\delta, \quad q_0=2\sqrt{q_{-1}q_{+1}} \quad \text{for } \Delta\theta=0, \quad (17)$$

$$p\equiv1, \quad q_{-1}=q_{+1} \quad \text{for } \Delta\theta=\pi. \quad (18)$$

In uniform space ($\Omega=0$), Eq. (16) possesses a solution with constant density, $n=\mu/p$. As shown in Refs. [7,11,15], such constant solutions to Eqs. (4) and (5) are modulationally stable only in the AFM phase, with $\delta>0$. Below, we will only consider the case of the AFM condensate (which, in particular, applies to the ^{23}Na condensate, with $\delta=3.14\times10^{-2}$). In the presence of a sufficiently weak trap, Eq. (16) can be solved approximately by means of the TF approximation [25]. In this way, neglecting the kinetic-energy term ($\sim\partial_x^2\sqrt{n}$) in Eq. (16), we find density profiles of the three spin components:
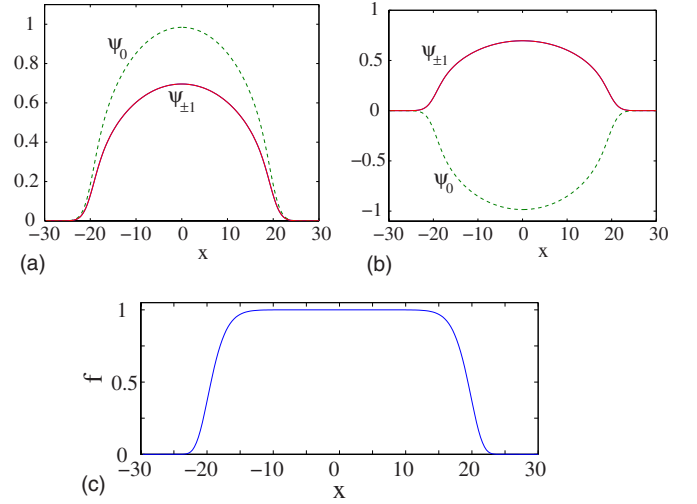
FIG. 1. (Color online) Top panels: Examples of two stable spin-polarized states for $\Delta\theta=0$ (left panel) and $\Delta\theta=\pi$ (right panel), both obtained for $\Omega=0.1$ and $\mu=2$. Wave functions $\psi_{\pm1}$ are identical and are depicted by the solid line, while the wave function ψ_0 is depicted by the dashed line. In the left panel, $q_{-1}=q_{+1}=0.5$ and $q_0=1$, while in the right panel $q_{-1}=q_{+1}=0.25$ and $q_0=0.5$. Bottom panel: The spatial distribution of the total mean-field spin f; note that in this case $f_y=f_z=0$ and $f_x=\pm f$ for $\Delta\theta=0$ or π, respectively.

$$n_j=\frac{q_j}{p}\left(\mu-\frac{1}{2}\Omega^2x^2\right), \quad (19)$$

in the spatial region $\frac{1}{2}\Omega^2x^2<\mu$, and $n_j=0$ elsewhere. Obviously, all three components of the TF solution have the same spatial width (the TF radius), $R_{\text{TF}}=\sqrt{2\mu}/\Omega$.

In numerical simulations, we used a fixed-point algorithm (the Newton-Raphson method) to find exact spin-polarized solutions to Eqs. (4) and (5), with profiles close to those produced by the TF approximation of Eq. (19). In particular, we used, as an initial guess, three identical profiles of the form

$$\psi_j(x)=\sqrt{n(x)}\exp(i\theta_j), \quad (20)$$

with $n(x)=\mu-\frac{1}{2}\Omega^2x^2$ and $\Delta\theta=0$ or π. Then, keeping the trap's strength, Ω, fixed, we varied the chemical potential μ, and the numerical solution converged to stable spin-polarized states, which were indeed close to the approximate one given by Eq. (19). Two typical examples are shown in the top panels of Fig. 1 for both cases, $\Delta\theta=0$ (left panel) and $\Delta\theta=\pi$ (right panel), with $\mu=2$. The numerically determined states are very close to their TF-predicted counterparts, with $q_{-1}=q_{+1}=0.5$ and $q_0=1$ ($\Delta\theta=0$, top left panel) and $q_{-1}=q_{+1}=0.25$ and $q_0=0.5$ ($\Delta\theta=\pi$, top right panel). The distributions of the spin components are time-independent with $f_y=f_z=0$, and $f_x=\pm f$ for $\Delta\theta=0$ or π, respectively. The total mean-field spin f is shown in the bottom panel of Fig. 1.

The stability of the TF states was examined too (by means of both the linear-stability analysis and direct simulations). It has been concluded that these states are always stable.
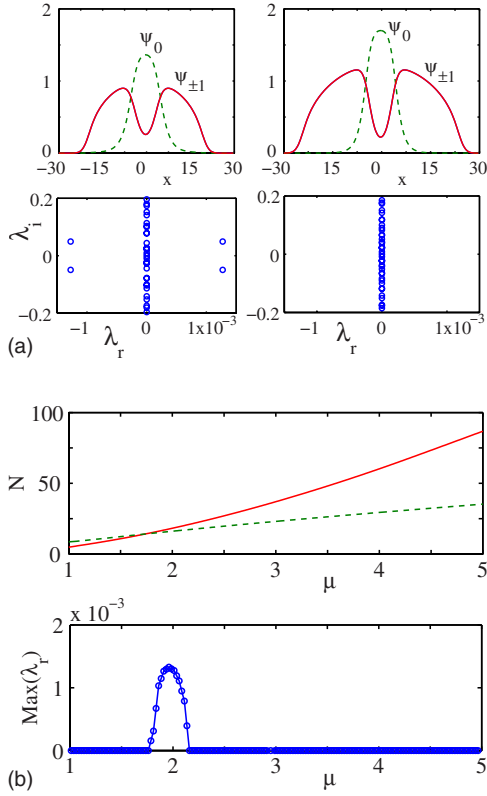
FIG. 2. (Color online) Spin-polarized state with a hole in the $\psi_{\pm1}$ components, and a pulselike shape of the ψ_0 field, for $\Omega=0.1$ and $\Delta\theta=0$. The top left and right panels show unstable and stable states, with $\mu=2$ and $\mu=3$, respectively; solid and dashed lines depict components $\psi_{\pm1}$ and ψ_0. The two panels in the second row display spectral planes (λ_r,λ_i) of the (in)stability eigenvalues for the same states. Note that the instability (of the state pertaining to $\mu=2$) is of the oscillatory type, being accounted for by a quartet of eigenvalues with nonzero real parts. The solid and dashed lines in the third-row panel show the normalized number of atoms (norm), N, in components $\psi_{\pm1}$ and ψ_0, respectively, as a function of chemical potential μ. The bottom panel shows the maximal growth rate, $\max(\lambda_r)$, as a function of μ, which reveals the instability window for $1.81\leq\mu\leq2.15$, with a maximum instability growth rate $(\lambda_r)_{\max}\approx1.3\times10^{-3}$ at $\mu\approx2$. The latter value corresponds to the unstable state shown in the top left panel.

IV. SPIN-POLARIZED STATES WITH HOLES

Apart from the smooth spin-polarized states of the TF type, there exist other ones, which feature holes in some of the components, or in all of them. An example of such states is shown in Fig. 2. As seen in the two top panels of this figure, the ψ_0 component is concentrated in the form of a pulse located at the trap's center, while the $\psi_{\pm1}$ components feature a large hole at the same spot. This shape is explained by the fact that the interaction between components is repulsive, hence a peak (hole) in ψ_0 ($\psi_{\pm1}$) induces a hole (peak) in $\psi_{\pm1}$ (ψ_0). The norm N of each component is shown, as a function of chemical potential μ, in the third-row panel of Fig. 2, and typical sets of the linear-stability eigenvalues for these states are displayed, for two different values of μ, in the second-row panels. The state with $\mu=3$ (top right) is
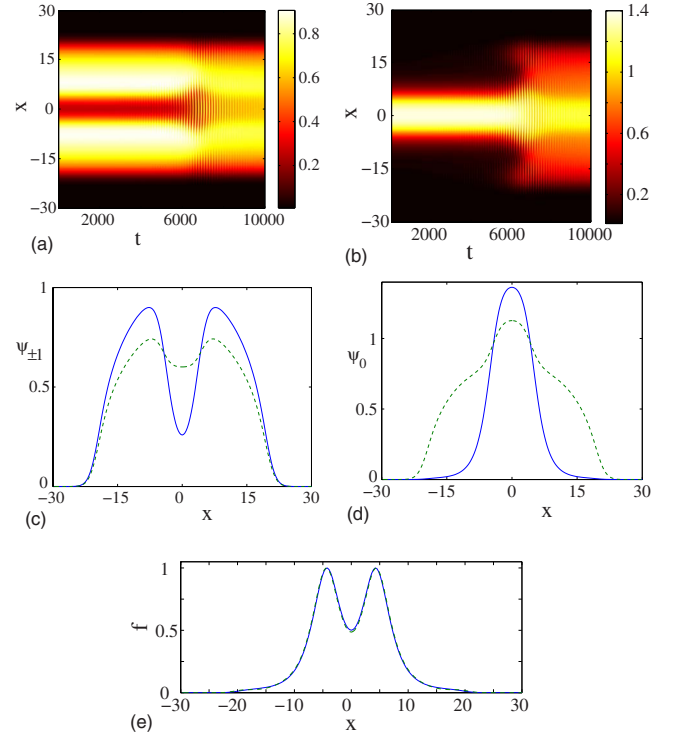
FIG. 3. (Color online) Top panels: Contour density plots display the evolution of the weakly unstable solution shown in Fig. 2 (the left and right panels represent, respectively, $\psi_{+1}\equiv\psi_{-1}$ and ψ_0 components). Because of the extremely small growth rate of the instability, it manifests itself only at $t>4000$. Middle panels: The respective wave-function profiles at $t=0$ (solid lines) and $t=10\,000$ (dashed lines); as above, the left and right panels show, respectively, wave functions $\psi_{\pm1}$ and ψ_0. Bottom panel: Snapshots of the distribution of the total mean-field spin $f=f_x$ at $t=0$ (solid line) and $t=10\,000$ (dashed line).

stable, as all the eigenvalues are imaginary, while the one with $\mu=2$ (top left panel) is unstable. Further analysis demonstrates that all such unstable states are destabilized by a *Hamiltonian Hopf bifurcation*, which gives rise to a quartet of eigenvalues with nonzero real parts. The instability interval is $1.81\leq\mu\leq2.15$, with the largest instability growth rate, $\max(\lambda_r)\approx1.3\times10^{-3}$, found at $\mu\approx2$ (see bottom panel of Fig. 2).

A similar state with the field profiles in $\psi_{\pm1}$ and ψ_0 exchanged, i.e., the ψ_0 component featuring the hole, and $\psi_{\pm1}$ ones concentrated in narrow pulses, were also found. Moreover, such states were found too with either ψ_0 or $\psi_{\pm1}$ having the opposite sign (i.e., for $\Delta\theta=\pi$). The results are not shown here, as the stability properties of these states are qualitatively the same as in the above case.

The evolution of unstable states is exemplified in Fig. 3, which displays results of direct simulations of Eqs. (4) and (5) for the unstable state with $\Delta\theta=0$ and $\mu=2$, that was presented in Fig. 2 (top left panel). In the top panels of Fig. 3, contour plots of densities of the components of the solution are displayed as a function of time (the densities of the ψ_{+1} and ψ_{-1} components are identical). It is clearly observed that the predicted oscillatory instability sets in at a very large time ($t\approx4000$, which corresponds to $t\approx5$ s in physical
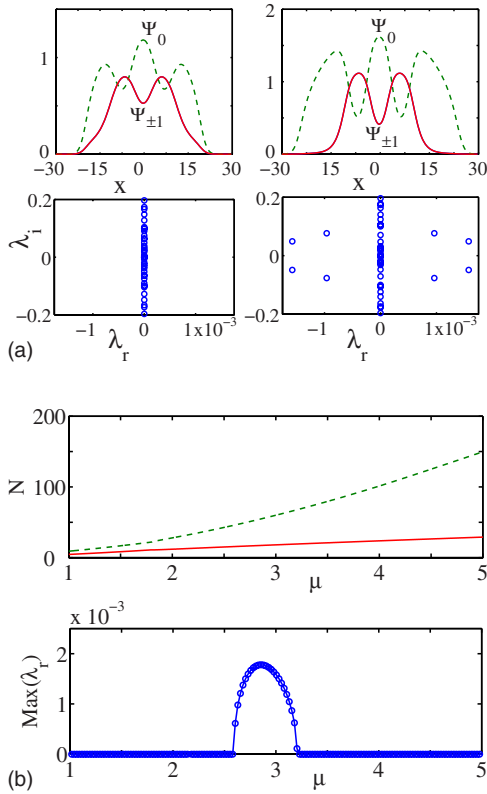
FIG. 4. (Color online) Same as Fig. 2 but for a state with one hole in each of the $\psi_{\pm 1}$ components and two holes in the ψ_0 component. In this case, the instability is driven by two quartets in the eigenvalue spectrum of small perturbations, which lead to instability in the interval $2.58 \leq \mu \leq 3.22$. The maximum instability growth rate is $\max(\lambda_r) \approx 1.8 \times 10^{-3}$ at $\mu \approx 2.9$. The unstable state shown in the top right panel corresponds to $\mu = 3$.

units); this is a consequence of the extremely small growth rate of the instability. Eventually, the system settles down to a steady state, which is qualitatively similar to the initial one. In particular, as seen in the top panels of Fig. 3, after $t \approx 8000$ the pulse in the ψ_0 component broadens and its amplitude accordingly decreases, while the hole in the $\psi_{\pm 1}$ components becomes shallower. This is clearly shown in the middle panels of Fig. 3, where snapshots of the spatial distributions of the wave functions at $t = 0$ (solid lines) and $t = 10\,000$ (dashed lines) are shown. Respective snapshots of the mean-field spin are also displayed in the bottom panel of Fig. 3; it is seen that the manifestation of the oscillatory instability does not affect f significantly. Note that here, as in the previous case with the TF polarized states, $f_y = f_z = 0$ and $f = f_x$.

Apart from the states considered above, it is also possible to find spin-polarized ones which feature, e.g., one hole in each of the $\psi_{\pm 1}$ components, and two holes in ψ_0. Examples of such a state are shown in the top panels of Fig. 4 (the left one, for $\mu = 2$, is stable, while the right one, for $\mu = 3$, is unstable). As seen in this figure, one may consider components ψ_{-1} and ψ_{+1} as built of two overlapping pulses, which induce two holes in the ψ_0 component due to the repulsive intercomponent interactions. Results of the stability analysis for these states are shown in Fig. 4. In this case, two quartets
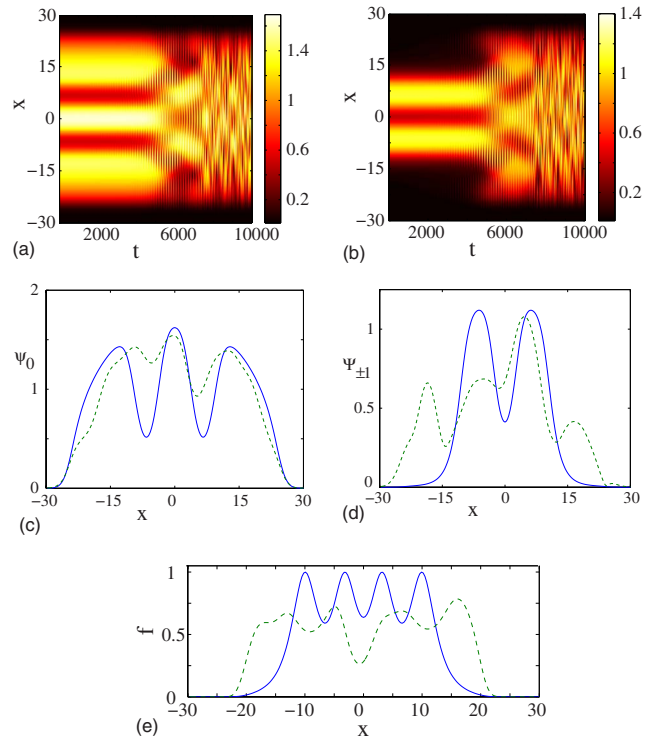
FIG. 5. (Color online) Same as Fig. 3, for the unstable state shown in the top right panel of Fig. 4 (it pertains to $\mu = 3$). The instability manifests itself at large times ($t > 3500$) and results in strong oscillatory deformation of the spinor condensate; this is clearly observed in the contour plots of the densities (top panels), the snapshots of the wave function profiles (middle panels), and the snapshots of the mean-field spin distribution (bottom panel).

of eigenvalues with nonzero real parts are found in the spectral plane (see the right panel in the second row of Fig. 4). These lead to instability in the interval $2.58 \leq \mu \leq 3.22$ (see
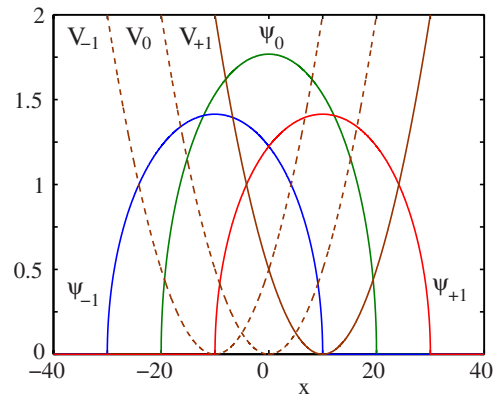
FIG. 6. (Color online) Initialization of the system when three spatially separated traps, V_{-1}, V_0 (shown by dashed parabolas), and V_{+1} (the solid parabola), with equal strengths ($\Omega = 0.1$) and centers placed at $x = -10$, 0, and $+10$, hold the TF states of the ψ_{-1}, ψ_0, and ψ_{+1} components, respectively. Then, two traps (V_{-1} and V_0), centered at $x = -10$ and $x = 0$, are turned off, and a stationary solution, supported solely by the trap (V_{+1}) centered at $x = 10$, is looked for by means of the fixed-point algorithm, using the configuration with the three mutually shifted components as an input.

the bottom panel in Fig. 4). The respective largest instability growth rate is $(\lambda_r)_{max} \approx 1.8 \times 10^{-3}$ for $\mu \approx 2.9$, i.e., of the same order of magnitude as in the previous case. The development of the instability was studied, as above, in direct simulations, starting with initial conditions in the form of a perturbed solution pertaining to $\mu=3$. The result is shown in Fig. 5, in terms of the evolution of identical densities of the $\psi_{\pm 1}$ components and the density of ψ_0. Again, the instability manifests itself at large times ($t > 3500$, which corresponds to $t > 4.2$ s in physical units), but in this case the final result is a strong oscillatory deformation of the three components (after $t \approx 5500$), contrary to the establishment of the new stationary pulse-hole state observed in Fig. 3. This deformation is clearly seen by the snapshots of the spatial distributions of the wave functions (middle panels of Fig. 5) and the mean-field spin (bottom panel of Fig. 5), at $t=0$ (solid lines) and $t=10\,000$ (dashed lines). Notice that the resulting states are asymmetric with respect to $x \rightarrow -x$ transformations, indicating the possibility of asymmetric states in the system such as domain walls (see also below).

Similar states with one hole in ψ_0 and *two holes* in each of the $\psi_{\pm 1}$ components, as well as their counterparts corresponding to $\Delta\theta=\pi$, have also been found. They are not shown here; as in the previous case, the (in)stability of these additional states is similar to that reported in Fig. 4.

V. DOMAIN WALLS

In the above sections, we reported the spin-polarized states in which all three spin components were spatially overlapping, since they were confined by the same potential trap. However, it is also possible to use three different traps, each confining a different component, to initially separate them, and then allow the system to evolve in the presence of only one of these traps (i.e., turning off the other two). In this section, we present spin-polarized states, including domain-wall (DW) structures, obtained in this way.

First, we describe the initialization of the system. We assume that the three TF-shaped components are initially
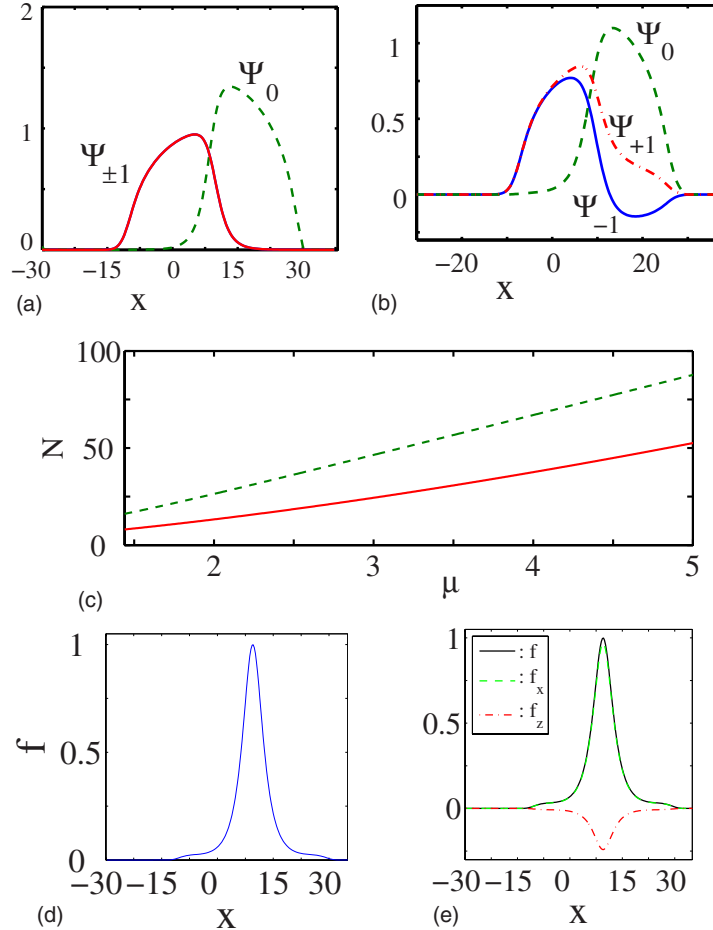
FIG. 7. (Color online) Top left panel: Wave functions of the components (ψ_{+1} and ψ_{-1} are identical) in a stationary state found from the initial configuration prepared as shown in Fig. 6. The resulting spin-polarized state has the form of a domain-wall structure between the ψ_0 and $\psi_{\pm 1}$ components. The parameters are $\Omega=0.1$ and $\mu=2$. The top right panel shows the wave functions of the domain-wall state found at $\mu=1.43$. Middle panel: The norm of each component in the domain-wall structure vs the chemical potential (the dependences for $\Delta\theta=0$ and π are identical). Bottom panels: The spatial distribution of the total mean-field spin (solid lines). For $\mu=2$ (bottom left) $f=f_x$, while for $\mu=1.43$ (bottom right) $f=\sqrt{f_x^2+f_z^2} \approx f_x$; in the latter case, the f_x and f_z components are depicted by dashed and dashed-dotted lines, respectively.
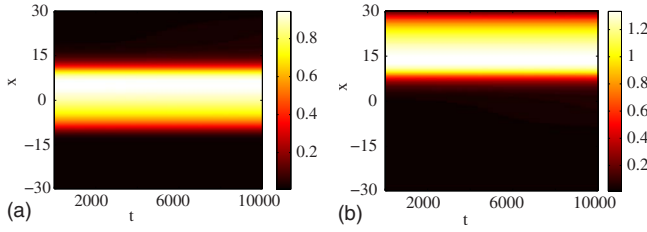
FIG. 8. (Color online) Evolution of the domain-wall structure shown in the top left panel of Fig. 7, to which a random perturbation was added. Shown in the left and right panels are spatiotemporal contour plots of the densities in components $\psi_{\pm1}$ (identical to each other) and ψ_0, respectively.

loaded into three different traps, $V_j(x)$, of the same strength, Ω, centered at different positions:

$$V_j(x) = \frac{1}{2}\Omega^2(x - j\Delta x)^2, \quad j = -1, \ 0, \ +1. \quad (21)$$

We choose $\Delta x = \Omega^{-1}$ (i.e., $\Delta x = 10$ for $\Omega = 0.1$), which induces the initially separated TF configurations; see Fig. 6.

After preparing this state, we turn off the traps $V_{-1}(x)$ and $V_0(x)$, keeping only the rightmost one, $V_{+1}(x)$, which now acts on all three components. The so defined initial configuration is fed, as an input, into the fixed-point algorithm, to find a spin-polarized state generated by it. Other possibilities, such as turning off potentials $V_{\pm1}$ and keeping V_0, arranging the three components in a different way, etc., eventually lead to retrieving the spin-polarized states presented in the previous sections, while the approach outlined above [keeping $V_{+1}(x)$ and switching $V_{-1}(x)$ and $V_0(x)$ off] generates new DW patterns, which are displayed in Fig. 7, and could not be obtained otherwise (in fact, the asymmetry of the procedure is instrumental in generating the new states).

The most interesting spin-polarized DW states found following this procedure correspond to values of the chemical potential $\mu \geq 1.43$ (or norm $N \geq 5400$), for $\Omega = 0.1$; for smaller μ, we typically found structures of the TF type. Two examples, one for $\mu = 2$, and another exactly corresponding to $\mu = 1.43$, are shown in Fig. 7.

In the former case ($\mu = 2$), the ψ_0 component (which has the larger norm) is centered to the right of the midpoint of the remaining trap ($x_{+1} = 10$), while the identical $\psi_{\pm1}$ components are pushed to the left, due to the repulsion from ψ_0, with a DW created between $\psi_{\pm1}$ and ψ_0. Note that the total

mean-field spin is $f = f_x$ and has a pulselike distribution shown in the bottom left panel of Fig. 7.

In the state found at the above-mentioned special value, $\mu = 1.43$, which is shown in the top right panel of Fig. 7, the shape of the ψ_0 component is similar to that displayed in the left top panel for $\mu = 2$, while the $\psi_{\pm1}$ components are *not* identical, in contrast to the previous example. In the present case, the ψ_0 and $\psi_{\pm1}$ components overlap over a wider spatial region, and ψ_{-1} changes its sign at $x \approx 13$, featuring a structure resembling the waveform of a dark soliton embedded in a bright one [26]. Notice that in this case f_z takes a small nonzero value and, thus, it has a small contribution to the total mean-field spin; however, in fact, as seen in the bottom-right panel of Fig. 7, the latter can be approximated as $f = \sqrt{f_x^2 + f_z^2} \approx f_x$.

The stability of the DW states was also investigated in the framework of the BdG equations. It was concluded that there are no unstable eigenvalues, i.e., with a nonzero real part, in interval $1.43 \leq \mu \leq 5$, or, equivalently, $5400 \leq N \leq 35\,000$ for $\Omega = 0.1$ (not shown here in detail). Thus the DWs are stable in this region. Verification of the stability, performed by direct simulations of Eqs. (4) and (5), is illustrated in Figs. 8 and 9, for $\mu = 2$ and $\mu = 1.43$, respectively. It is obvious that these states indeed remain stable at very large times exceeding $t = 10\,000$ (i.e., 12 s in physical units).

VI. CONCLUSIONS

In this work, we have studied spin-polarized states in antiferromagnetic spinor ($F = 1$) Bose-Einstein condensates. In particular, our analysis applies to a quasi-1D spinor condensate of sodium atoms. The considerations were based on analytical calculations and numerical computations of the coupled Gross-Pitaevskii equations for this setting.

Assuming that all three hyperfine (spin) components are confined in the same harmonic trap, we have found various types of spin-polarized states and examined their stability. The first family consists of Thomas-Fermi configurations, considered analytically in the framework of the single-mode approximation (which assumes the similarity of the spatial profiles of all the components). Within their existence region, these states were found to be stable. Also identified were more complex patterns, which include states composed of one or more pulselike structures in one component, that induce holes in the other components, and states with holes in all three components. These states feature windows of weak
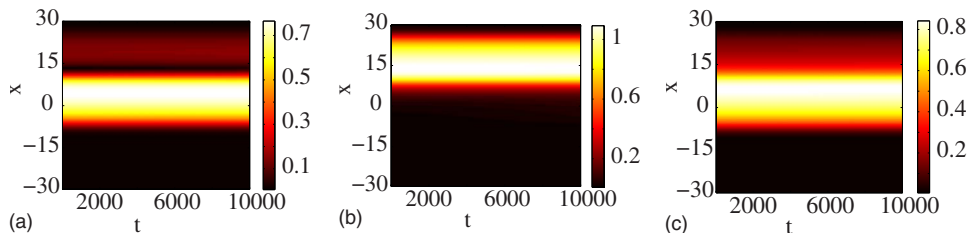
FIG. 9. (Color online) Same as Fig. 8 but for the state shown in the top right panel of Fig. 7. The left, middle, and right panels show, respectively, the densities in the ψ_{-1}, ψ_0, and ψ_{+1} components. Noteworthy is a stationary dark-soliton-like structure, located at $x \approx 13$ in the ψ_{-1} component.

instability. The development of the instability was investigated by means of direct numerical simulations, which demonstrate that it manifests itself at very long times, and results in a deformation of the states with a single hole in some of the components, which does not qualitatively change their form, and a stronger (oscillatory) perturbation and a potential eventual asymmetry of the states with multiple hoels.

Fully stable families of spin-polarized states develop from configurations consisting of initially separated components (that are held in three mutually shifted traps). These states form domain-wall structures between the components, at values of the chemical potential above a certain threshold. Just at the threshold we have found another spin-polarized state in which all the components partly overlap.

It would definitely be interesting to investigate the existence and stability of higher-dimensional counterparts of the 1D spin-polarized states found in this work. In this connection, a relevant question for further analysis is whether spinor condensates support stable topological objects, such as dark solitons or vortices. Moreover, the effect of temperature on the statics and dynamics of the spin-polarized states presented in this work is certainly another challenging issue deserving further investigation. Work in these directions is in progress.

[1] D. M. Stamper-Kurn and W. Ketterle, e-print arXiv:cond-mat/0005001.

[2] D. M. Stamper-Kurn, M. R. Andrews, A. P. Chikkatur, S. Inouye, H.-J. Miesner, J. Stenger, and W. Ketterle, Phys. Rev. Lett. **80**, 2027 (1998).

[3] M.-S. Chang, C. D. Hamley, M. D. Barrett, J. A. Sauer, K. M. Fortier, W. Zhang, L. You, and M. S. Chapman, Phys. Rev. Lett. **92**, 140403 (2004).

[4] J. Stenger, S. Inouye, D. M. Stamper-Kurn, H.-J. Miesner, A. P. Chikkatur, and W. Ketterle, Nature (London) **396**, 345 (1998).

[5] A. E. Leanhardt, Y. Shin, D. Kielpinski, D. E. Pritchard, and W. Ketterle, Phys. Rev. Lett. **90**, 140403 (2003).

[6] J. Ieda, T. Miyakawa, and M. Wadati, Phys. Rev. Lett. **93**, 194102 (2004); J. Phys. Soc. Jpn. **73**, 2996 (2004).

[7] L. Li, Z. Li, B. A. Malomed, D. Mihalache, and W. M. Liu, Phys. Rev. A **72**, 033611 (2005).

[8] W. Zhang, Ö. E. Müstecaplioglu, and L. You, Phys. Rev. A **75**, 043601 (2007).

[9] M. Uchiyama, J. Ieda, and M. Wadati, J. Phys. Soc. Jpn. **75**, 064002 (2006).

[10] B. J. Dabrowska-Wüster, E. A. Ostrovskaya, T. J. Alexander, and Y. S. Kivshar, Phys. Rev. A **75**, 023617 (2007).

[11] H. E. Nistazakis, D. J. Frantzeskakis, P. G. Kevrekidis, B. A. Malomed, and R. Carretero-González, arXiv:0705.1324.

[12] H. Pu, C. K. Law, S. Raghavan, J. H. Eberly, and N. P. Bigelow, Phys. Rev. A **60**, 1463 (1999); H. Pu, S. Raghavan, and N. P. Bigelow, *ibid.* **61**, 023602 (2000).

[13] T.-L. Ho, Phys. Rev. Lett. **81**, 742 (1998).

[14] S. Yi, Ö. E. Müstecaplioglu, C. P. Sun, and L. You, Phys. Rev. A **66**, 011601(R) (2002).

[15] N. P. Robins, W. Zhang, E. A. Ostrovskaya, and Y. S. Kivshar, Phys. Rev. A **64**, 021601(R) (2001).

[16] I. M. Merhasin, B. A. Malomed, and Y. B. Band, Phys. Rev. A **74**, 033614 (2006).

[17] V. M. Pérez-García, H. Michinel, and H. Herrero, Phys. Rev. A **57**, 3837 (1998); L. Salasnich, A. Parola, and L. Reatto, *ibid.* **65**, 043614 (2002); **66**, 043603 (2002).

[18] T. Ohmi and K. Machida, J. Phys. Soc. Jpn. **67**, 1822 (1998).

[19] E. G. M. van Kempen, S. J. J. M. F. Kokkelmans, D. J. Heinzen, and B. J. Verhaar, Phys. Rev. Lett. **88**, 093201 (2002).

[20] N. N. Klausen, J. L. Bohn, and C. H. Greene, Phys. Rev. A **64**, 053602 (2001).

[21] W. Zhang, S. Yi, and L. You, Phys. Rev. A **70**, 043611 (2004).

[22] J. Mur-Petit, M. Guilleumas, A. Polls, A. Sanpera, M. Lewenstein, K. Bongs, and K. Sengstock, Phys. Rev. A **73**, 013629 (2006).

[23] M. Moreno-Cardoner, J. Mur-Petit, M. Guilleumas, A. Polls, A. Sanpera, and M. Lewenstein, Phys. Rev. Lett. **99**, 020404 (2007).

[24] H. Saito and M. Ueda, Phys. Rev. A **72**, 023610 (2005).

[25] L. P. Pitaevskii and S. Stringari, *Bose-Einstein Condensation* (Oxford University Press, Oxford, 2003).

[26] P. G. Kevrekidis, D. J. Frantzeskakis, B. A. Malomed, A. R. Bishop, and I. G. Kevrekidis, New J. Phys.. **5**, 64 (2003).